





Simulating the spin-boson model with a controllable reservoir in an ion trap

G.-X. Wang ^{1,*} Y.-K. Wu ^{1,2,*} R. Yao,³ W.-Q. Lian,³ Z.-J. Cheng ¹ Y.-L. Xu,¹ C. Zhang,¹ Y. Jiang,¹ Y.-Z. Xu,¹ B.-X. Qi,¹ P.-Y. Hou ^{1,2} Z.-C. Zhou,^{1,2} L. He,^{1,2} and L.-M. Duan^{1,2,4,†}

¹*Center for Quantum Information, Institute for Interdisciplinary Information Sciences, Tsinghua University, Beijing 100084, People's Republic of China*

²*Hefei National Laboratory, Hefei 230088, People's Republic of China*

³*HYQ Co., Ltd., Beijing 100176, People's Republic of China*

⁴*New Cornerstone Science Laboratory, Beijing 100084, People's Republic of China*



(Received 12 February 2024; revised 19 March 2024; accepted 15 May 2024; published 3 June 2024)

The spin-boson model is a prototypical model for open quantum dynamics. Here we simulate the spin-boson model using a chain of trapped ions in which a spin is coupled to a structured reservoir of bosonic modes. We engineer the spectral density of the reservoir by adjusting the ion number, the target ion location, the laser detuning to the phonon sidebands, and the number of frequency components in the laser, and we observe their effects on the collapse and revival of the initially encoded information. Our work demonstrates that the ion trap is a powerful platform for simulating open quantum dynamics with complicated reservoir structures.

DOI: [10.1103/PhysRevA.109.062402](https://doi.org/10.1103/PhysRevA.109.062402)

I. INTRODUCTION

Quantum simulation is an important tool to understand quantum many-body physics [1–3] and is one of the most promising applications of noisy intermediate-scale analog or digital quantum computers [4]. Typical digital quantum computers use two-level spins as the basic processing unit and encode other particles like fermions and bosons through, e.g., the Jordan-Wigner transformation [5] or the standard binary encoding with a truncation in the particle number [6,7]. In contrast, analog quantum simulators can directly utilize the bosonic degrees of freedom and largely save the complexity of encoding and thus are preferable for near-term study of hybrid systems like spin-boson coupled systems.

Spin-boson coupled models are fundamental physical models for describing the matter-light interaction and various couplings to the bath in materials. For a single spin and a single bosonic mode, the well-known quantum Rabi model [8] and Jaynes-Cummings model [9] are used. For multiple spins coupled to the same bosonic mode, one uses the Dicke model [10,11] and the Tavis-Cummings model [12], and if one further extends the model to multiple bosonic modes, they are generalized to the Rabi-Hubbard model [13–15] and the Jaynes-Cummings-Hubbard model [16–19]. On the other hand, one can also consider a single spin coupled to multiple bosonic modes, which is known as the spin-boson model [20] and is a prototypical model for understanding open quantum dynamics like the dissipation of an atom in an environment of electromagnetic field modes or of a solid-state qubit in a bath.

Within a continuum of the bosonic modes (a reservoir), the spin dynamics can be solved analytically [20] or numerically

[21–26], and interesting phenomena like the non-Markovian revival of information [27–29] have been observed. However, directly solving the spin dynamics for strong coupling or discrete spectra can still be challenging. Experimentally, this model has been simulated in systems like superconducting circuits [29,30] and neutral atoms or quantum dots in photonic crystals [31–33]. As one of the leading platforms for quantum simulation, ion traps have been used to realize many spin-boson coupled models [34–40]. Proposals for the spin-boson model have also been made in the ion-trap system [41,42] but have not yet been realized. Here we simulate the spin-boson model in a chain of trapped ions, which naturally hosts a set of collective phonon modes with a configurable structure and supports laser-induced coupling between the spin and phonon modes. Specifically, we generate a spin-phonon interaction for a target ion in a chain of up to 20 ions and demonstrate the collapse and revival of the initially encoded information. We engineer the reservoir structure using the ion number, the location of the target ion, and the spin-phonon detuning and by introducing multiple frequency components in the spin-phonon coupling, and we observe their effects on the simulated open quantum dynamics. Our work demonstrates that trapped ions are an ideal platform for simulating spin-boson coupled models and provides tools for future study of complicated coupling patterns.

II. SETUP

Our setup is sketched in Fig. 1. A linear chain of $N = 20$ $^{171}\text{Yb}^+$ ions is held in a cryogenic blade trap with a transverse trap frequency $\omega_x = 2\pi \times 2.397$ MHz. We encode the spin state in the $|0\rangle \equiv |^2S_{1/2}, F = 0, m_F = 0\rangle$ and $|1\rangle \equiv |^2S_{1/2}, F = 1, m_F = 0\rangle$ levels of a selected ion. Due to the Coulomb interaction between the ions, their transverse oscillations couple to N collective phonon modes within a band

*These authors contributed equally to this work.

†lmduan@tsinghua.edu.cn

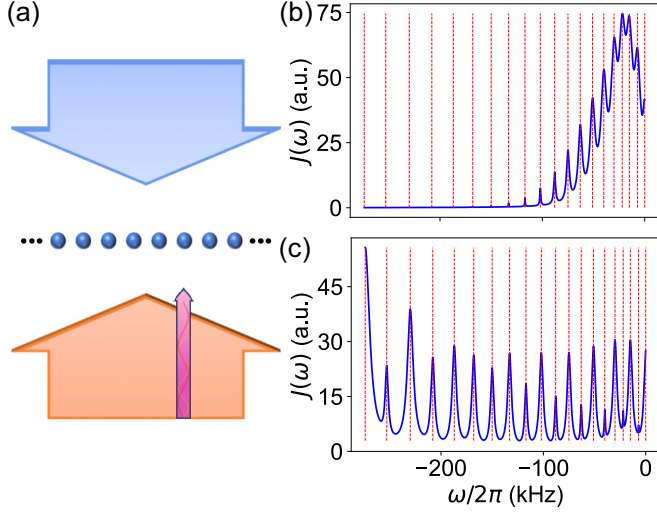


FIG. 1. (a) Experimental scheme. We use a counterpropagating 355-nm laser for Raman transitions, with a global beam for the sideband cooling of the whole ion chain and a narrow beam for the spin-phonon interaction on a selected ion. The narrow beam with a beam-waist radius of $3\ \mu\text{m}$ can move along the chain to address any target ion controlled by an acousto-optic deflector. Other standard lasers for the basic operations, such as Doppler cooling, optical pumping, and the qubit state detection, are not shown. (b) The theoretical phonon spectrum in arbitrary units seen by an edge ion weighted by the spin-phonon coupling strength [Eq. (2)]. Here we set a sideband Rabi rate $\eta_k\Omega = 2\pi \times 6.67\ \text{kHz}$ for the COM mode, which is the coupling strength we use in the following experiments. (c) A similar plot for a central ion.

of about $\Delta\omega_x \sim e^2/(4\pi\epsilon_0 m\omega_x d^3)$, where m and e are the mass and charge of the ion and d is the average ion spacing. With a pair of counterpropagating 355-nm global Raman laser beams, we can perform sideband cooling to all the transverse modes [43]. In this experiment, due to the misalignment of the trap electrode (see Appendix A), we have a relatively large heating rate of a few hundred quanta per second for the phonon modes close to the center-of-mass (c.m.) mode, thus leading to a relatively high phonon number between 0.3 and 0.9 after sideband cooling. Nevertheless, this does not hinder our observation of the spin dynamics and may actually enhance the effective spin-phonon coupling to allow us to cover more phonon modes, as we will see below.

We can use a global laser beam and a counterpropagating focused laser beam to form a Raman transition on the target ion near the red motional sideband and to couple its spin state with the local phonon mode, which in turn can be expanded to the N collective modes. The relevant spin-boson Hamiltonian of the system thus reads

$$H = \frac{\Delta}{2}\sigma_z + \sum_{k=1}^N \omega_k a_k^\dagger a_k + \Omega \sum_{k=1}^N \eta_k b_k (\sigma_+ a_k + \sigma_- a_k^\dagger), \quad (1)$$

where Δ and ω_k are the frequencies of the spin and the phonon modes in the rotating frame and Ω is the carrier Rabi frequency of the Raman transition. a_k and a_k^\dagger are the annihilation and creation operators of the k th phonon mode with the Lamb-Dicke parameter η_k , and b_k is the corresponding

mode coefficient for the target ion. Note that the spin and the phonon frequencies can be shifted by the same constant without affecting any dynamics. Therefore, from now on we will use the frequency of the c.m. mode as the reference and set it to zero.

If we regard the phonon modes as a reservoir, the open quantum dynamics of the spin is governed by a spectral density function $J(\omega) \equiv \pi \sum_k \lambda_k^2 \delta(\omega - \omega_k)$ [20,42], which takes into account the coupling strength $\lambda_k \equiv 2\eta_k b_k \Omega$ to each mode and the number of modes around each frequency ω . As shown by the vertical dashed lines in Fig. 1(b), the collective mode frequencies of a linear ion chain in a harmonic trap naturally exhibit a structured spectrum which is denser near the c.m. mode and is sparser on the low-frequency end. By choosing a target ion at different locations on the chain and thus different b_k 's, we further modulate the spectral density via the coupling strength to different modes, as shown in Figs. 1(b) and 1(c). Here we replace the δ function in the spectral density function by a Lorentzian line shape to cover the power broadening [43]

$$J(\omega) = \sum_k \frac{|2\eta_k b_k \Omega|^3 / \sqrt{2}}{(\omega - \omega_k)^2 + (2\eta_k b_k \Omega)^2 / 2}, \quad (2)$$

where we set the linewidth to be $2\eta_k b_k \Omega$, which is the red-sideband coupling strength of a single mode when the phonon number is zero. In practice, with a nonzero average phonon number, these peaks further broaden, and we shall be able to couple to more phonon modes. Note that this spectrum is not directly used in later numerical simulations. Its purpose is just to visualize the reservoir engineering and to guide the choice of parameters in the following experiments.

III. NON-MARKOVIAN DYNAMICS AND RESERVOIR ENGINEERING

First, we demonstrate the non-Markovian spin dynamics in the phonon reservoir under the spin-phonon interaction. As shown in Fig. 2(a), we initialize an edge ion in orthogonal states $|0\rangle$ and $|1\rangle$ using the 355-nm Raman laser, and we turn on the spin-phonon coupling with a sideband Rabi rate $\eta_k\Omega = 2\pi \times 6.67\ \text{kHz}$ in the c.m. mode and a spin frequency $\Delta = -2\pi \times 20\ \text{kHz}$ in the dense region of the phonon spectrum in Fig. 1(b). We evolve the system for time t and display the final population of the spin in $|1\rangle$ as the yellow squares and green triangles for initial states $|1\rangle$ and $|0\rangle$ in Fig. 2(a), respectively. Initially, these two orthogonal states are easily distinguishable up to the 2% detection error and the 3% state preparation error due to the axial motion of the ion and the pointing of the narrow laser. As the system evolves, the encoded information gradually leaks into the phonon reservoir, and the two states can no longer be distinguished. This is reflected in Fig. 2(a) as the flat region near zero for the blue data points, which is the absolute difference between the populations from the two initial states. However, because of the finite and discrete phonon modes, as well as the fact that the dynamics is much faster than the motional decoherence on the timescale of milliseconds, the information in the reservoir can still flow backwards into the spin before it is eventually lost into the larger environment. This can be seen as the revival peak in the blue data points around $t_r = 0.18\ \text{ms}$. We can also verify this

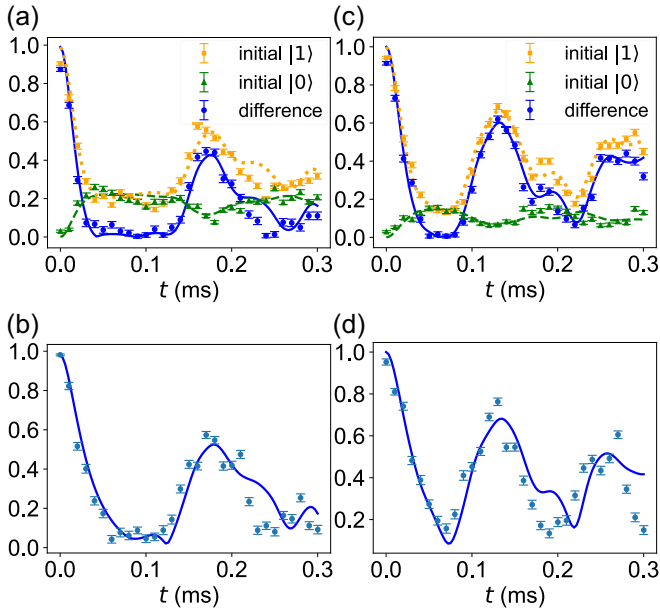


FIG. 2. Non-Markovian spin dynamics. (a) Probability of finding an edge ion in a chain of $N = 20$ ions in $|1\rangle$ when evolved from the initial state of $|1\rangle$ (yellow squares) or $|0\rangle$ (green triangles) and their absolute difference (blue circles). Here we tune the spin frequency to the dense part $\Delta = -2\pi \times 20$ kHz of the phonon spectrum in Fig. 1(b). The two states quickly become indistinguishable as the initially encoded information leaks to the phonon modes, but then the information flows backwards due to the discrete nature of the reservoir. Theoretical curves are computed by truncating to the dominant phonon modes as described in Appendix D. (b) A similar plot for the edge ion from the initial state of $|+\rangle$ and $|-\rangle$. Here we perform quantum state tomography for the final spin states and compute their trace distance. Similar collapse and revival are observed for the information encoded in the superposition basis. (c) and (d) Similar plots for an edge ion in a chain of $N = 10$ ions with roughly the same ion spacing. The revival becomes more significant due to the sparser reservoir spectrum. Error bars represent one standard deviation from 300 trials.

experimental result with a numerical simulation based on the calibrated experimental parameters. Due to the exponential increase in the Hilbert-space dimension under finite (thermal) phonon numbers, a direct calculation with even a moderate truncation of the phonon numbers will be challenging, so we further truncate the number of involved phonon modes based on their detuning and the relative coupling strength (see Appendix D for more details). As shown by the curves in Fig. 2, we obtain good agreement between the experimental and theoretical results without fitting parameters, thus confirming the successful quantum simulation of the spin-boson model.

The collapse and revival of the information occur not only in the $|0\rangle$ or $|1\rangle$ (particle number) basis but also in the $|+\rangle$ or $|-\rangle$ (superposition) basis. In Fig. 2(b) we initialize the spin state in $|+\rangle$ and $|-\rangle$ by a $\pi/2$ pulse of the Raman laser. Then we repeat the above process to evolve the system under the spin-boson model Hamiltonian, and we perform quantum state tomography for the final spin states ρ_{\pm} from the two initial states by measuring the expectation values of σ_x , σ_y ,

and σ_z . By definition, the maximal retrievable information can be given by their trace distance $D(\rho_+, \rho_-)$ [44]. As we can see, in this case the initial decay of the information is slower since, ideally, the dephasing time T_2 for the spontaneous emission will be twice the relaxation time T_1 in the particle-number basis. Nevertheless, we can observe a similar flat region around zero and a revival peak at roughly the same time of $t_r = 0.18$ ms, which confirms the phase coherence of the revival signal. Note that if we move to a rotating frame at the spin frequency by setting $\Delta = 0$ in Eq. (1) and shift the phonon frequencies accordingly, we can immediately see that the two initial states from $|0\rangle$ or $|1\rangle$ have the same energy, such that there will be no phase shift with respect to the bare resonant frequency of the spin at the revival time. Therefore, ideally, the revival in the $|+\rangle$ or $|-\rangle$ basis should occur right at the same time as the $|0\rangle$ or $|1\rangle$ basis by the superposition principle.

Next, we demonstrate our capability to manipulate the spectral density of the reservoir. One straightforward way is to adjust the ion number. Ideally, if we increase the ion number while keeping the average ion spacing unchanged, we can expect there to be more and more phonon modes in the fixed band of $\Delta\omega_x$. In Figs. 2(c) and 2(d), we compare the above results with $N = 10$ ions at roughly the same ion spacing by raising the axial trap frequency. Specifically, we place the spin frequency at the same location $\Delta = -2\pi \times 20$ kHz of the phonon spectrum. Here the initial information leakage rate does not change significantly as the decreased mode number is compensated by the increased mode coefficients b_k . However, due to the sparser phonon modes, we can clearly see that the revival of the information gets faster and stronger.

In practice, it is often difficult to keep increasing the ion number in a linear chain while maintaining a constant ion spacing: Due to the experimental noise, the ion number in a one-dimensional chain is usually below 100 for a room-temperature trap [45–47] and below 200 for a cryogenic trap [48,49]. Although it is also possible to utilize the transverse modes of a two-dimensional (2D) ion crystal in a Paul trap [50–54] or a Penning trap with suitable individual addressing [55], it is desirable to have more flexible ways to manipulate the structure of the phonon reservoir. In Fig. 3(a) we engineer the spectral density $J(\omega)$ by tuning the frequency of the spin $\Delta \rightarrow \Delta'$. As we can see from Eq. (1), this is equivalent to a shift in the frequency of all the phonon modes and thus a corresponding shift in the spectral density in Eq. (2) as $J(\omega) \rightarrow J(\omega - \Delta + \Delta')$. Specifically, we set $\Delta' = -2\pi \times 50$ kHz in a sparser and weaker region of the phonon spectrum for $N = 20$ ions in Fig. 1(b). In this case, the leakage of the information into the reservoir becomes much slower. Again, the decay for the $|0\rangle$ or $|1\rangle$ basis is faster than that for the $|+\rangle$ or $|-\rangle$ basis, and again, we observe the revival signal after a flat basin in the information.

According to Eq. (2), another method of reservoir engineering is to place the target spin at different locations on the chain, hence modifying the mode coefficients b_k . In Fig. 3(b), we move the narrow Raman laser to a central ion of the $N = 20$ chain and repeat the above experimental sequence. From a comparison of Figs. 1(b) and 1(c), we can see that for the edge ion, the coupling is mainly concentrated at the high-frequency end near the c.m. mode and the spectrum is nearly

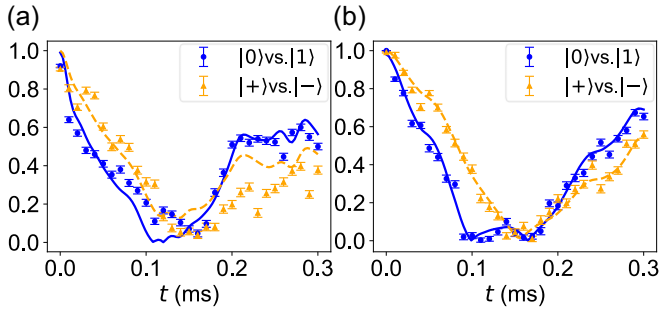


FIG. 3. Reservoir engineering by a single-frequency laser. (a) By tuning the frequency of the Raman laser, we place the edge ion into a sparser region of the phonon reservoir $\Delta = -2\pi \times 50$ kHz with weaker coupling strength. Again, we use the absolute difference for $|0\rangle$ and $|1\rangle$ and the trace distance for $|+\rangle$ and $|-\rangle$ to quantify the remaining information. (b) By focusing the addressing laser on a central ion, we change the spin-phonon coupling pattern in Fig. 1(c) such that the coupling gets weaker in the dense region into the environment slows down, and the backflow of information gets much higher. Error bars represent one standard deviation from 300 trials.

continuous in the densest region, while for the central ion the coupling is more uniform and displays a discrete feature for the same spin-phonon interaction strength. Also note that near the c.m. mode in Fig. 1(c), the coupling to the odd modes is suppressed owing to the reflection symmetry of the ion chain, which effectively further increases the separation between the relevant phonon modes. Therefore, we can expect a slower leakage of the encoded information in the spin and a stronger revival, as we observe in the experiment.

From the above examples, we see that the coupling of the spin to the phonon reservoir is often inefficient in the sense that only a small fraction of the phonon modes can be coupled. This is because within our achievable parameter regime, often, the coupling strength $\eta_k \Omega$ below $2\pi \times 10$ kHz is much smaller than the width of the phonon band above $2\pi \times 100$ kHz. (To become narrower, the phonon band requires larger ion distances and weaker axial trapping, making the system more sensitive to the experimental noise, as we mention above.) Also we can see this from our numerical simulation method, in which truncation to only a few nearby phonon modes is sufficient for convergence. On the one hand, this suggests that we may need a large number of ions to approximate a continuous phonon spectrum. On the other hand, this fact also provides us with further adjustability of the spectrum by adding more frequency components in the driving laser to couple to the other unused phonon modes.

To demonstrate this idea, we choose two frequency components in the narrow Raman laser beam separated by $\delta = 2\pi \times 20$ kHz. Each frequency component generates a spin-boson Hamiltonian in the form of Eq. (1), and their joint effect is just to combine the two spectra which are separated by δ , as shown in Fig. 4(a). Note that strictly speaking, this picture is incorrect because the two frequency components couple to the same set of phonon modes and should be treated coherently. However, as long as the coupling strength to the individual phonon mode $\eta_k b_k \Omega$ is much weaker than the

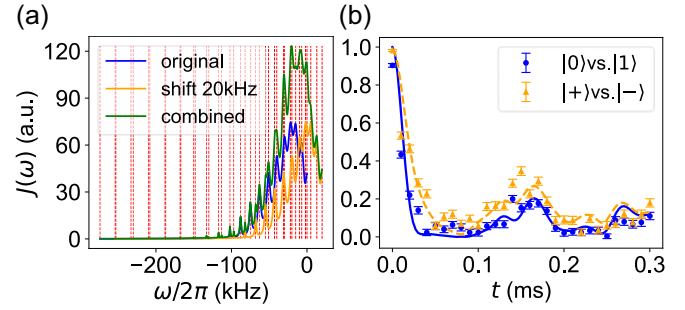


FIG. 4. Reservoir engineering by a bichromatic coupling laser. (a) The phonon spectrum seen by an edge ion [blue, the same as in Fig. 1(b)] and that for a laser shifted by $\delta = 2\pi \times 20$ kHz (orange). The vertical dashed lines indicate the locations of the two sets of phonon modes. Since the frequency separation δ is much larger than the coupling strength $\eta_k b_k \Omega$, the two sets of spectra can add up incoherently to give the green curve. (b) In the dense region of the combined spectrum $\Delta = -2\pi \times 20$ kHz, the decay becomes even faster than in Fig. 2, and the revival becomes less significant. Again, we use the absolute difference for $|0\rangle$ and $|1\rangle$ and the trace distance for $|+\rangle$ and $|-\rangle$ to quantify the remaining information. Error bars represent one standard deviation from 300 trials.

frequency separation δ , the two frequency components will never excite the same phonon mode significantly at the same time. Then our approximate model will be valid. Here, to maintain consistency with the previous results, we choose the same coupling strength $\eta_k \Omega = 2\pi \times 6.67$ kHz to the c.m. mode for both frequency components. From the combined spectral density (green curve) in Fig. 4(a), we expect denser phonon modes with stronger coupling strength. This is consistent with the experimental and numerical results in Fig. 4(b), where we get faster leakage of the information and a weaker revival signal.

IV. CONCLUSION

To sum up, we simulated a spin-boson model in a linear chain of trapped ions and studied the open quantum dynamics of a spin in a structured reservoir. We demonstrated the strong controllability of the spectral density of the reservoir using various degrees of freedom, including the ion number, the target ion location, the laser detuning to the phonon sidebands, and the number of frequency components in the laser. We observed a change in the collapse and revival of the encoded information under the reservoir engineering, and we confirmed the experimental results with numerical simulations. Our work provides convenient tools to engineer complicated bosonic reservoir for spins and thus to solve spin dynamics that are challenging for classical computers, and our method can be readily generalized to a 2D ion crystal to further increase the ion number and to produce more complex coupling patterns. It is also convenient to introduce more spins into the model by adding more focused laser beams on different ions, which will allow the study of multiple emitters in a shared bosonic environment. Finally, stronger controllability of the bosonic environment can also be obtained by adding active heating via stochastic kicks [56] or sympathetic sideband cooling on some ions.

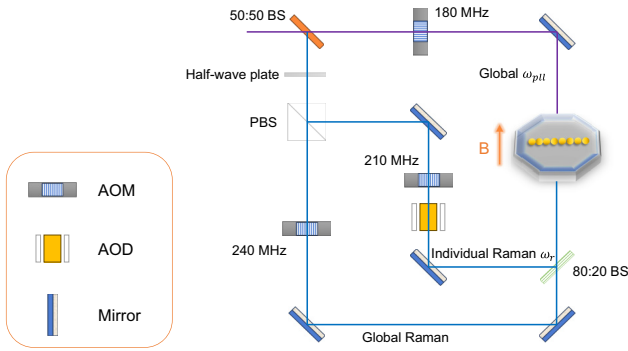


FIG. 5. Optical paths for the global and individual 355-nm Raman beams.

ACKNOWLEDGMENTS

This work was supported by the Innovation Program for Quantum Science and Technology (Grant No. 2021ZD0301601), the Tsinghua University Initiative Scientific Research Program, and the Ministry of Education of China. L.-M.D. acknowledges additional support from the New Cornerstone Science Foundation through the New Cornerstone Investigator Program. Y.-K.W. acknowledges additional support from the Tsinghua University Dushi program and the startup fund. C.Z. acknowledges additional support from a Tsinghua University Shuimu Scholar postdoctoral fellowship.

APPENDIX A: EXPERIMENTAL SETUP

We trap a chain of $^{171}\text{Yb}^+$ ions in a cryogenic trap with segmented blade electrodes [49] and an rf frequency $\omega_{\text{rf}} = 2\pi \times 35.733$ MHz. A magnetic field of $B = 5.5$ G perpendicular to the axial direction of the trap is used to define the quantization axis. We follow the standard procedure to use a 369.5-nm laser for Doppler cooling, optical pumping, and qubit state detection [57], and we use counterpropagating 355-nm Raman laser beams (Paladin Compact 355-4000 with a repetition rate of 118.7 MHz) to couple the spin and the phonon modes. As shown in Fig. 5, the frequency and the phase of each 355-nm beam can further be adjusted by an acousto-optic modulator (AOM). The 355-nm laser beams are oriented at 45° to the transverse x and y directions. We use elliptic global Raman beams for sideband cooling of the ion chain, and an additional narrow beam with a Gaussian waist radius (where the intensity drops to $1/e^2$) of $3 \times 5 \mu\text{m}^2$ to generate the spin-boson model and to prepare the initial state of the target spin. The orientation of the narrow beam can be controlled by an acousto-optic deflector (AOD) to select different target ions.

For a chain of $N = 20$ ions, we adjust the axial confinement to achieve an average ion spacing of about $4.6 \mu\text{m}$. We can read the ions' locations on a CCD camera with an accuracy of about $0.6 \mu\text{m}$. To further improve the accuracy, we can use the frequencies of the transverse phonon modes to fit the ion spacing [40]. Then we can compute the phonon mode vectors and thus obtain b_k 's for the target ion.

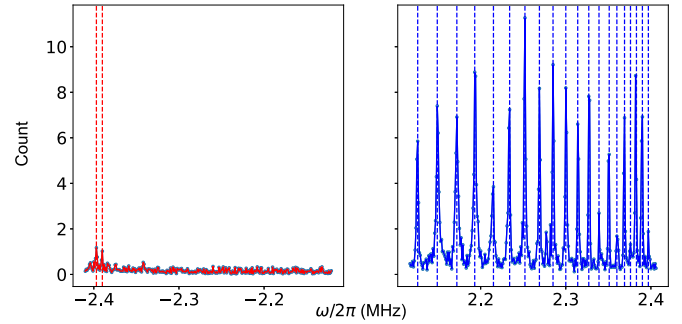


FIG. 6. Spectra of the red and blue sidebands for $N = 20$ ions under a weak global Raman laser. Vertical dashed lines represent the positions of the phonon modes. For the red sideband, only the c.m. mode and the tilt mode have a visible population.

Our blade electrodes are aligned symmetrically when assembled at room temperature. However, after cooling down to the cryogenic temperature at 6 K, some components deform differently, resulting in the misalignment of these individual electrodes. In particular, one of the dc blades gets closer to the trap center, leading to a higher heating rate. Also there is tilt in the electrodes, causing a nonuniform electric field over the ion chain and thus heating of phonon modes other than the c.m. mode.

APPENDIX B: SIDEBAND COOLING

Before each experimental trial, we initialize the motional state by 3-ms Doppler cooling. Then we perform 9.75-ms sideband cooling for the x and y modes by sequentially cooling different frequencies. The spectra of the red and blue motional sidebands under the same weak driving [40] are shown in Fig. 6 for $N = 20$ ions. As we can see, apart from the c.m. mode and the adjacent tilt mode, all other modes have been cooled to a low phonon number below 0.3.

We further measure the phonon number for the c.m. mode and the tilt mode by comparing the blue- and red-sideband dynamics under a narrow Raman laser on the edge ion. With a weak driving strength, the off-resonant coupling to all the other phonon modes can be neglected, and effectively, we get a Jaynes-Cummings model. We can thus estimate the average phonon number by comparing the blue and red motional sidebands [43] as shown in Fig. 7. This gives us $\bar{n} = 0.9$ for the c.m. mode and $\bar{n} = 0.5$ for the tilt mode.

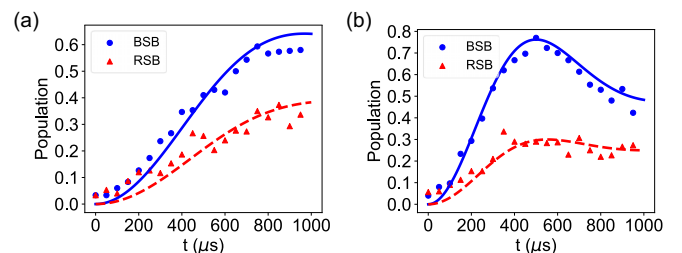


FIG. 7. Blue- and red-sideband dynamics for (a) the c.m. mode and (b) the tilt mode with a narrow Raman laser on the edge ion.

We attribute the higher phonon number of c.m. and tilt modes to their higher heating rates (about 1000 quanta per second for the c.m. mode and about 500 quanta per second for the tilt mode). For the c.m. mode, it is well known that the heating rate will scale linearly with the ion number if the heating is mainly caused by a uniform electric-field noise across the ion chain. In practice, the electric-field noise will have slow spatial variations, so we can expect decreasing effects on phonon modes with lower frequencies and smaller spatial wavelengths [58]. In this experiment, due to the misalignment of the trap electrode described in Appendix A, we expect a relatively large spatial variation of the electric field, which contributes to the heating rate of the tilt mode.

APPENDIX C: QUANTUM STATE TOMOGRAPHY

To compare the dynamics of the spin-boson model from the initial states $|0\rangle$ and $|1\rangle$, we simply measure the final spin state in the $|0\rangle$ and $|1\rangle$ basis σ_z . To compare the dynamics from initial states in the $|+\rangle$ and $|-\rangle$ superposition basis σ_x , we further need to perform quantum state tomography for the density matrix of the spin and to compute the trace distance $D(\rho_+, \rho_-) = \frac{1}{2} \text{Tr} |\rho_+ - \rho_-|$.

To reconstruct the spin density matrix, we measure the expectation values of σ_x , σ_y , and σ_z to get $\rho = (I + \sum_i \langle \sigma_i \rangle \sigma_i)/2$. Among these observables, σ_z can directly be measured in the $|0\rangle$ and $|1\rangle$ basis. To measure σ_x , we apply a $\pi/2$ pulse on the target ion using a Raman laser with the same phase as the one used to prepare the initial $|+\rangle$ and $|-\rangle$ states. As for σ_y , we shift the phase of the $\pi/2$ pulse by an additional $\pi/2$.

APPENDIX D: NUMERICAL SIMULATION

In this Appendix we describe how we numerically simulate the dynamics of the spin-boson model with one spin and N bosonic modes. Due to the exponential increase in the Hilbert-space dimension, even if we truncate each collective mode to a moderate phonon number of $n_{\text{cut}} = 3$, the total dimension of the system can still scale as $2(n_{\text{cut}} + 1)^N = 2^{41} \approx 2 \times 10^{12}$ for $N = 20$ modes. However, for our typical phonon number of 0.3–0.9 for each mode, there is still a non-negligible probability for them to have a phonon number above this truncation.

Inspired by the fact that our driving laser is able to couple to only a few adjacent phonon modes satisfying $|2\eta_k b_k \Omega| \gtrsim |\Delta - \omega_k|$, we can discard the phonon modes that are not significantly excited by the spin-phonon interaction. Specifically, we give a weight $[2\eta_k b_k \Omega / (\Delta - \omega_k)]^2$ to each mode k and keep only the K modes with the largest weight. Here K is a hyperparameter. In practice, we can gradually increase K and check whether the result has converged. For the numerical simulation relevant to this experiment, often, we find a truncation between 5 and 10 to be sufficient.

Next, we observe that the Hamiltonian (1) conserves the total particle number. Therefore, given an initial Fock state of one spin and K phonon modes, its time evolution is restricted in a subspace of dimension

$$D = C(M + K - 1, K - 1) + C(M + K - 2, K - 1), \quad (\text{D1})$$

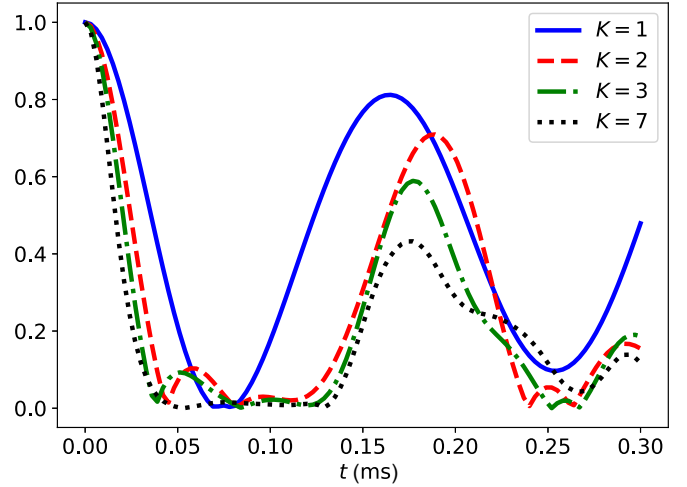


FIG. 8. Absolute difference between spin dynamics from $|0\rangle$ and $|1\rangle$ in Fig. 2(a) when truncating to different numbers of phonon modes K . Each curve is averaged over $S = 100$ trials for the initial phonon number distribution.

where M is the total excitation number of the initial Fock state and $C(n, m) \equiv n!/[m!(n-m)!]$ is the combination number to choose m items from n elements. This allows us to express the Hamiltonian in a more compact and efficient way. For an initial superposition state of the spin, we can compute the dynamics in the two subspaces individually and then combine them together coherently to obtain the reduced density matrix of the spin.

Finally, we assume that initially, the phonon modes are in thermal states with the average phonon number given by the measured value in the experiment. Specifically, for $N = 20$ ions we set the average phonon number for the c.m. mode to be 0.9, that of the tilt mode to be 0.5, and that of all the remaining modes to be 0.3. For $N = 10$ ions we have better sideband cooling, so we simply choose $\bar{n} = 0.2$ for all the modes, which also comes from comparing the red and blue motional sideband spectra, similar to Fig. 6. We randomly generate $S = 100$ trials for the initial phonon number distribution and average over them to obtain the numerical results for the spin dynamics. Note that in the numerical simulation we consider only a finite initial phonon number and neglect the heating effect during the evolution. This is because for a heating rate up to hundreds of quanta per second and an evolution time up to 300 μs , the increase in the average phonon number will be on the order of only about 0.1 per mode, which is smaller than the existing phonon number in these modes.

As an example, in Fig. 8 we show the numerical results for the absolute difference between the dynamics from $|0\rangle$ and $|1\rangle$ in Fig. 2(a) when truncating to different numbers of phonon modes K . As we can see, typically, including the dominant two or three phonon modes can provide a good explanation of the position of the major revival peak, while more phonon modes are still needed to explain its height, as well as the other smaller features in the spin dynamics.

- [1] R. P. Feynman, Simulating physics with computers, *Feynman and Computation* (CRC Press, Boca Raton, FL, 2018), pp. 133–153.
- [2] I. M. Georgescu, S. Ashhab, and F. Nori, Quantum simulation, *Rev. Mod. Phys.* **86**, 153 (2014).
- [3] J. I. Cirac and P. Zoller, Goals and opportunities in quantum simulation, *Nat. Phys.* **8**, 264 (2012).
- [4] K. Bharti, A. Cervera-Lierta, T. H. Kyaw, T. Haug, S. Alperin-Lea, A. Anand, M. Degroote, H. Heimonen, J. S. Kottmann, T. Menke, W.-K. Mok, S. Sim, L.-C. Kwek, and A. Aspuru-Guzik, Noisy intermediate-scale quantum algorithms, *Rev. Mod. Phys.* **94**, 015004 (2022).
- [5] P. Jordan and E. Wigner, Über das paulische äquivalenzverbot, *Z. Phys.* **47**, 631 (1928).
- [6] N. P. D. Sawaya, T. Menke, T. H. Kyaw, S. Johri, A. Aspuru-Guzik, and G. G. Guerreschi, Resource-efficient digital quantum simulation of d-level systems for photonic, vibrational, and spin-s Hamiltonians, *npj Quantum Inf.* **6**, 49 (2020).
- [7] R. D. Somma, G. Ortiz, E. H. Knill, and J. Gubernatis, Quantum simulations of physics problems, *Proc. SPIE* **5105**, 96 (2003).
- [8] P. Forn-Díaz, L. Lamata, E. Rico, J. Kono, and E. Solano, Ultrastrong coupling regimes of light-matter interaction, *Rev. Mod. Phys.* **91**, 025005 (2019).
- [9] E. T. Jaynes and F. W. Cummings, Comparison of quantum and semiclassical radiation theories with application to the beam maser, *Proc. IEEE* **51**, 89 (1963).
- [10] K. Hepp and E. H. Lieb, On the superradiant phase transition for molecules in a quantized radiation field: The Dicke maser model, *Ann. Phys. (NY)* **76**, 360 (1973).
- [11] Y. K. Wang and F. T. Hioe, Phase transition in the Dicke model of superradiance, *Phys. Rev. A* **7**, 831 (1973).
- [12] M. Tavis and F. W. Cummings, Exact solution for an N -molecule–radiation-field Hamiltonian, *Phys. Rev.* **170**, 379 (1968).
- [13] M. Schiró, M. Bordyuh, B. Öztop, and H. E. Türeci, Phase transition of light in cavity QED lattices, *Phys. Rev. Lett.* **109**, 053601 (2012).
- [14] M.-J. Hwang and M.-S. Choi, Large-scale maximal entanglement and Majorana bound states in coupled circuit quantum electrodynamic systems, *Phys. Rev. B* **87**, 125404 (2013).
- [15] G. Zhu, S. Schmidt, and J. Koch, Dispersive regime of the Jaynes–Cummings and Rabi lattice, *New J. Phys.* **15**, 115002 (2013).
- [16] A. D. Greentree, C. Tahan, J. H. Cole, and L. C. L. Hollenberg, Quantum phase transitions of light, *Nat. Phys.* **2**, 856 (2006).
- [17] D. G. Angelakis, M. F. Santos, and S. Bose, Photon-blockade-induced Mott transitions and XY spin models in coupled cavity arrays, *Phys. Rev. A* **76**, 031805(R) (2007).
- [18] M. J. Hartmann, F. G. S. L. Brandão, and M. B. Plenio, Strongly interacting polaritons in coupled arrays of cavities, *Nat. Phys.* **2**, 849 (2006).
- [19] D. Rossini and R. Fazio, Mott-insulating and glassy phases of polaritons in 1D arrays of coupled cavities, *Phys. Rev. Lett.* **99**, 186401 (2007).
- [20] A. J. Leggett, S. Chakravarty, A. T. Dorsey, M. P. A. Fisher, A. Garg, and W. Zwerger, Dynamics of the dissipative two-state system, *Rev. Mod. Phys.* **59**, 1 (1987).
- [21] R. Egger and C. H. Mak, Low-temperature dynamical simulation of spin-boson systems, *Phys. Rev. B* **50**, 15210 (1994).
- [22] R. Bulla, T. A. Costi, and T. Pruschke, Numerical renormalization group method for quantum impurity systems, *Rev. Mod. Phys.* **80**, 395 (2008).
- [23] J. Prior, A. W. Chin, S. F. Huelga, and M. B. Plenio, Efficient simulation of strong system-environment interactions, *Phys. Rev. Lett.* **105**, 050404 (2010).
- [24] B. Peropadre, D. Zueco, D. Porras, and J. J. García-Ripoll, Nonequilibrium and nonperturbative dynamics of ultrastrong coupling in open lines, *Phys. Rev. Lett.* **111**, 243602 (2013).
- [25] Y. Yao, L. Duan, Z. Lü, C.-Q. Wu, and Y. Zhao, Dynamics of the sub-Ohmic spin-boson model: A comparison of three numerical approaches, *Phys. Rev. E* **88**, 023303 (2013).
- [26] A. González-Tudela and J. I. Cirac, Quantum emitters in two-dimensional structured reservoirs in the nonperturbative regime, *Phys. Rev. Lett.* **119**, 143602 (2017).
- [27] H.-P. Breuer, E.-M. Laine, and J. Piilo, Measure for the degree of non-Markovian behavior of quantum processes in open systems, *Phys. Rev. Lett.* **103**, 210401 (2009).
- [28] U. Hoeppe, C. Wolff, J. Küchenmeister, J. Niegemann, M. Drescher, H. Benner, and K. Busch, Direct observation of non-Markovian radiation dynamics in 3D bulk photonic crystals, *Phys. Rev. Lett.* **108**, 043603 (2012).
- [29] V. S. Ferreira, J. Banker, A. Sipahigil, M. H. Matheny, A. J. Keller, E. Kim, M. Mirhosseini, and O. Painter, Collapse and revival of an artificial atom coupled to a structured photonic reservoir, *Phys. Rev. X* **11**, 041043 (2021).
- [30] O. Astafiev, A. M. Zagoskin, A. A. Abdumalikov, Yu. A. Pashkin, T. Yamamoto, K. Inomata, Y. Nakamura, and J. S. Tsai, Resonance fluorescence of a single artificial atom, *Science* **327**, 840 (2010).
- [31] J. D. Thompson, T. G. Tiecke, N. P. de Leon, J. Feist, A. V. Akimov, M. Gullans, A. S. Zibrov, V. Vuletić, and M. D. Lukin, Coupling a single trapped atom to a nanoscale optical cavity, *Science* **340**, 1202 (2013).
- [32] A. Goban, C.-L. Hung, S.-P. Yu, J. D. Hood, J. A. Muniz, J. H. Lee, M. J. Martin, A. C. McClung, K. S. Choi, D. E. Chang, O. Painter, and H. J. Kimble, Atom–light interactions in photonic crystals, *Nat. Commun.* **5**, 3808 (2014).
- [33] M. Arcari, I. Söllner, A. Javadi, S. Lindskov Hansen, S. Mahmoodian, J. Liu, H. Thyrrstrup, E. H. Lee, J. D. Song, S. Stobbe, and P. Lodahl, Near-unity coupling efficiency of a quantum emitter to a photonic crystal waveguide, *Phys. Rev. Lett.* **113**, 093603 (2014).
- [34] D. Lv, S. An, Z. Liu, J.-N. Zhang, J. S. Pedernales, L. Lamata, E. Solano, and K. Kim, Quantum simulation of the quantum Rabi model in a trapped ion, *Phys. Rev. X* **8**, 021027 (2018).
- [35] M.-L. Cai, Z.-D. Liu, W.-D. Zhao, Y.-K. Wu, Q.-X. Mei, Y. Jiang, L. He, X. Zhang, Z.-C. Zhou, and L.-M. Duan, Observation of a quantum phase transition in the quantum Rabi model with a single trapped ion, *Nat. Commun.* **12**, 1126 (2021).
- [36] Q.-X. Mei, B.-W. Li, Y.-K. Wu, M.-L. Cai, Y. Wang, L. Yao, Z.-C. Zhou, and L.-M. Duan, Experimental realization of the Rabi-Hubbard model with trapped ions, *Phys. Rev. Lett.* **128**, 160504 (2022).
- [37] K. Toyoda, Y. Matsuno, A. Noguchi, S. Haze, and S. Urabe, Experimental realization of a quantum phase transition of polaritonic excitations, *Phys. Rev. Lett.* **111**, 160501 (2013).
- [38] R. Ohira, S. Kume, K. Takayama, S. Muralidharan, H. Takahashi, and K. Toyoda, Blockade of phonon hopping in

- trapped ions in the presence of multiple local phonons, *Phys. Rev. A* **103**, 012612 (2021).
- [39] S. Debnath, N. M. Linke, S.-T. Wang, C. Figgatt, K. A. Landsman, L.-M. Duan, and C. Monroe, Observation of hopping and blockade of Bosons in a trapped ion spin chain, *Phys. Rev. Lett.* **120**, 073001 (2018).
- [40] B.-W. Li, Q.-X. Mei, Y.-K. Wu, M.-L. Cai, Y. Wang, L. Yao, Z.-C. Zhou, and L.-M. Duan, Observation of non-Markovian spin dynamics in a Jaynes-Cummings-Hubbard model using a trapped-ion quantum simulator, *Phys. Rev. Lett.* **129**, 140501 (2022).
- [41] D. Porras, F. Marquardt, J. von Delft, and J. I. Cirac, Mesoscopic spin-boson models of trapped ions, *Phys. Rev. A* **78**, 010101(R) (2008).
- [42] A. Lemmer, C. Cormick, D. Tamascelli, T. Schaetz, S. F. Huelga, and M. B. Plenio, A trapped-ion simulator for spin-boson models with structured environments, *New J. Phys.* **20**, 073002 (2018).
- [43] D. Leibfried, R. Blatt, C. Monroe, and D. Wineland, Quantum dynamics of single trapped ions, *Rev. Mod. Phys.* **75**, 281 (2003).
- [44] M. A. Nielsen and I. L. Chuang, *Quantum Computation and Quantum Information*, 10th ed. (Cambridge University Press, Cambridge, 2010).
- [45] J. Zhang, G. Pagano, P. W. Hess, A. Kyprianidis, P. Becker, H. Kaplan, A. V. Gorshkov, Z.-X. Gong, and C. Monroe, Observation of a many-body dynamical phase transition with a 53-qubit quantum simulator, *Nature (London)* **551**, 601 (2017).
- [46] M. K. Joshi, C. Kokail, R. van Bijnen, F. Kranzl, T. V. Zache, R. Blatt, C. F. Roos, and P. Zoller, Exploring large-scale entanglement in quantum simulation, *Nature (London)* **624**, 539 (2023).
- [47] B.-W. Li, Y.-K. Wu, Q.-X. Mei, R. Yao, W.-Q. Lian, M.-L. Cai, Y. Wang, B.-X. Qi, L. Yao, L. He, Z.-C. Zhou, and L.-M. Duan, Probing critical behavior of long-range transverse-field Ising model through quantum Kibble-Zurek mechanism, *PRX Quantum* **4**, 010302 (2023).
- [48] G. Pagano, P. W. Hess, H. B. Kaplan, W. L. Tan, P. Richerme, P. Becker, A. Kyprianidis, J. Zhang, E. Birkelbaw, M. R. Hernandez, Y. Wu, and C. Monroe, Cryogenic trapped-ion system for large scale quantum simulation, *Quantum Sci. Technol.* **4**, 014004 (2018).
- [49] R. Yao, W.-Q. Lian, Y.-K. Wu, G.-X. Wang, B.-W. Li, Q.-X. Mei, B.-X. Qi, L. Yao, Z.-C. Zhou, L. He, and L.-M. Duan, Experimental realization of a multiqubit quantum memory in a 218-ion chain, *Phys. Rev. A* **106**, 062617 (2022).
- [50] B. Szymanski, R. Dubessy, B. Dubost, S. Guibal, J.-P. Likforman, and L. Guidoni, Large two dimensional Coulomb crystals in a radio frequency surface ion trap, *Appl. Phys. Lett.* **100**, 171110 (2012).
- [51] A. Kato, A. Goel, R. Lee, Z. Ye, S. Karki, J. J. Liu, A. Nomerotski, and B. B. Blinov, Two-tone Doppler cooling of radial two-dimensional crystals in a radio-frequency ion trap, *Phys. Rev. A* **105**, 023101 (2022).
- [52] D. Kiesenhofer, H. Hainzer, A. Zhdanov, P. C. Holz, M. Bock, T. Ollikainen, and C. F. Roos, Controlling two-dimensional Coulomb crystals of more than 100 ions in a monolithic radio-frequency trap, *PRX Quantum* **4**, 020317 (2023).
- [53] M. Qiao, Z. Cai, Y. Wang, B. Du, N. Jin, W. Chen, P. Wang, C. Luan, E. Gao, X. Sun, H. Tian, J. Zhang, and K. Kim, Tunable quantum simulation of spin models with a two-dimensional ion crystal, *Nat. Phys.* **20**, 623 (2024).
- [54] S. A. Guo, Y. K. Wu, J. Ye, L. Zhang, W. Q. Lian, R. Yao, Y. Wang, R. Y. Yan, Y. J. Yi, Y. L. Xu, B. W. Li, Y. H. Hou, Y. Z. Xu, W. X. Guo, C. Zhang, B. X. Qi, Z. C. Zhou, L. He, and L. M. Duan, A site-resolved two-dimensional quantum simulator with hundreds of trapped ions, [arXiv:2311.17163](https://arxiv.org/abs/2311.17163) [Nature (London)(to be published)].
- [55] A. M. Polloreno, A. M. Rey, and J. J. Bollinger, Individual qubit addressing of rotating ion crystals in a penning trap, *Phys. Rev. Res.* **4**, 033076 (2022).
- [56] M. Kang, H. Nuomin, S. N. Chowdhury, J. L. Yuly, K. Sun, J. Whitlow, J. Valdiviezo, Z. Zhang, P. Zhang, D. N. Beratan, and K. R. Brown, Seeking a quantum advantage with trapped-ion quantum simulations of condensed-phase chemical dynamics, *Nat. Rev. Chem.* **8**, 340 (2024).
- [57] S. Debnath, A programmable five qubit quantum computer using trapped atomic ions, Ph.D. thesis, University of Maryland, 2016.
- [58] K. A. Landsman, Y. Wu, P. H. Leung, D. Zhu, N. M. Linke, K. R. Brown, L. Duan, and C. Monroe, Two-qubit entangling gates within arbitrarily long chains of trapped ions, *Phys. Rev. A* **100**, 022332 (2019).